Coronene diimide-based 'bowl' nanostructures as red emitters for the analysis of latent fingerprints and metal ion detection†

Prabhpreet Singh [ID] * and Poonam Sharma

We report an NIR-based photoluminescent material, namely benzo-coronene diimide (**CDI 2**), and its use in the visualization of latent fingerprints (LFPs) and in the metal ion detection in an aqueous medium. **CDI 2** exhibited nano-sized interlinked fibre structures forming 'bowl' shaped nanoarchitectures as red emitters with the Commission Internationale de l'Eclairage (CIE) coordinates (x, y) of (0.67, 0.33) with 100% colour purity in the solid state. **CDI 2** was confirmed to be the potential candidate for the analysis of LFPs and the detection of Pd^{2+}/Cu^{2+} in an aqueous medium.

Nowadays, latent (invisible) fingerprints are utilized as a personal identification mark in numerous instances to decrypt information during criminal and forensic investigations, to access computers and equipments utilized for administrative purposes, to provide aid in health and medical facilities, to mark the attendance of employees in government and private institutes and to monitor the entry/exit in security rooms owing to national interest.[1,2] Each and every individual, even the identical twins, have a unique pattern of friction ridges formed from the epidermis of the fingertips.[3] Different imaging techniques are used to visualize the LFPs; however, low resolution, destruction of the fingerprints during the analysis and low sensitivity of these techniques reduce the effectiveness of the LFPs.[4-6] The power-dusting technique, which involves the use of NIR-photoluminescent materials, emerged as a new advanced approach to develop the latent fingerprints.[7,8]

The availability of fluorescent red emitters is relatively limited in comparison with green and blue emitters for their application in organic light emitting diodes (OLEDs) due to their colour impurities.[9] According to previous literature, red OLEDs are available, which are based on either organometallic complexes or organic materials, such as dicyanomethylene, polyarene and chromene dopants.[10a,b] Therefore, the focus of the current research is in developing new red emitters for LFPs and metal ion sensing.[11a,b] Blue, green and red emitters are equally essential for the generation of white light. However, research over the past decade demonstrated high external quantum efficiencies of green and red emitters with a high colour purity and brightness compared with those of the blue triplet emitters. The characteristics of saturated red emission, spectral stability and stable electroluminescence efficiency of red emitters at high brightness and current enable them to be used as an emitting species in OLEDs. Herein, we report on benzocoronene[12,13] (**CDI 2**), which exhibited a highly conjugated π-system with emission extended to the red region (red emitters).[14,15] **CDI 2** (Fig. 1a) exhibited nano-sized interlinked fibre structures forming a 'bowl' like nanoarchitecture and was used to lift the LFPs developed on glass, metal, or aluminium surfaces. The CIE 1931 (RGB) coordinates[16] demonstrated a 100% colour purity in the solid state and on LFPs. **CDI 2** could be a potential candidate for the detection of Pd^{2+}/Pd^0 in water.

The preparation of the building block commenced with the Suzuki coupling reaction of 1-bromo-N,N′-di-(3-pentyl)-perylene 3,4,9,10-tetracarboxylic diimide with 4-formylphenylboronic acid, which was then subjected to condensation with hydroxylamine hydrochloride (Schiff-base condensation). Subsequent propargylation with propargyl bromide provided **PDI 1** in good yield.[11b] **CDI 2** was subsequently obtained through the photocyclization of **PDI 1** in CH_3CN (96% yield). The chemical structure of **CDI 2** was elucidated explicitly via 1D NMR (^{1}H and ^{13}C), 2D NMR (COSEY) and FTIR techniques (Fig. S1a–e†). **CDI 2** exhibited solubility in common organic solvents. The thermal stability of **CDI 2** was measured via the thermogravimetric analysis (TGA). **CDI 2** showed an initial mass loss of ~35% in the temperature range of 170–450 °C. This mass loss corresponds to the removal of propargyl and oxime moieties from **CDI 2**. The decomposition temperature (T_d, 60% weight loss) of **CDI 2** was found to be 550 °C (Fig. 1e).

The computational study was performed at the B3LYP/6-31G* basis level using the Gaussian 09 software. The contour picture of HOMO/LUMO revealed that the electron density of the HOMO localized predominately on the π-conjugated

Department of Chemistry, UGC Centre for Advanced Studies, Guru Nanak Dev University, Amritsar 143 005, India. E-mail: prabhpreet.chem@gndu.ac.in; Tel: +91-84271-01534
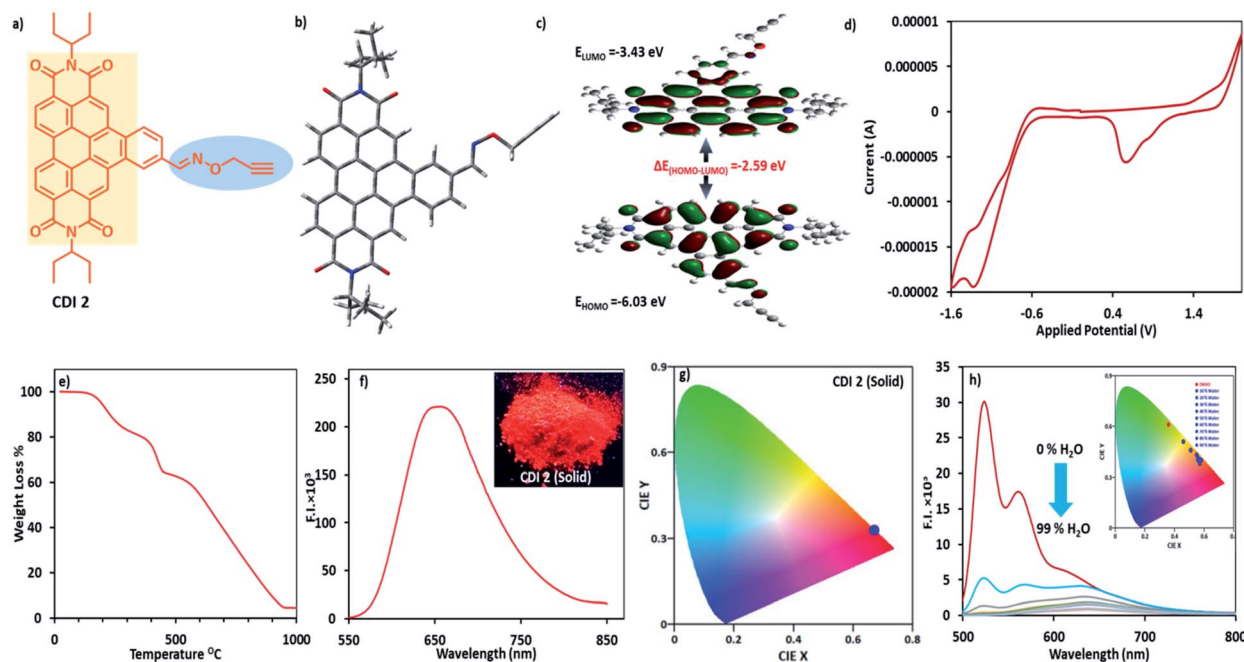
Fig. 1 (a) Structure of the **CDI 2** derivative; (b) energy optimized structure of **CDI 2**; (c) molecular plots of HOMO and LUMO of **CDI 2** using the DFT calculation at the B3LYP/6-31G* basis set; (d) cyclic voltammogram (CV) of **CDI 2** (0.2 mM) in the CH_2Cl_2 solvent; supporting electrolyte 0.1 mol L^{-1} TBAP; scan rate 0.05 V s^{-1}; potential range of −1.6–2.0 V vs. Ag/Ag+ electrode; (e) TGA curve of **CDI 2**; (f) emission spectrum of the fluorescent powder **CDI 2**; (g) CIE-1931 plots corresponding to the emission data of (f); (h) emission spectra of **CDI 2** (10 μM) in different ratios of H_2O and DMSO (λ_{ex} = 450 nm, slit width (ex/em) = 5/5) [inset of 1f showing photograph of **CDI 2** as solid powder; inset of 1 h showing CIE plot of various water ratios].

benzocoronene and oxygen heteroatom of the oxime moiety, while that of LUMO was mainly distributed on the benzocoronene part. The calculated HOMO and LUMO energy levels were −6.03 and −3.43 eV, respectively. The band gap energy in **CDI 2** was 2.59 eV (Fig. 1b, c, S2† and 3a).

In cyclic voltammetry, **CDI 2** exhibited an onset reduction (E_{red}) and weak oxidation potential (E_{ox}) values of 0.56 V and 1.39 V, respectively. The HOMO and LUMO energy levels calculated using the formula $E_{LUMO} = -[E_{red}(\text{onset}) + 4.4]$ eV and $E_{HOMO} = -[E_{ox}(\text{onset}) + 4.4]$ eV from experimentally determined E_{ox} and E_{red} values were −5.80 eV and −3.43 eV, respectively, which were in line with the HOMO–LUMO energies calculated via the density functional theory (Fig. 1d). The onset reduction peaks at −1.39 V and −1.6 V could be assigned to the second and third reductions of **CDI 2** characteristic for the π-conjugated system.

The introduction of more planar groups into **CDI 2** shifted the solid-state emission (powder form and thin film) to the red region with a λ_{em} of 660 nm (Fig. 1f) and a photoluminescence quantum yield of 3.89%. The emission wavelength of **CDI 2** was further complimented by considering the CIE-1931 RGB colour coordinates. The colour purity[17] of **CDI 2** in the powder form was calculated using the following equation:

$$\text{Colour purity} = \sqrt{\frac{(x_s - x_i)^2 + (y_s - y_i)^2}{(x_d - x_i)^2 + (y_d - y_i)^2}} \times 100\%$$

where (x_s, y_s) are the coordinates of the **CDI 2** sample at an emission wavelength of 650 nm, whereas (x_d, y_d) and (x_i, y_i) are the coordinates of the illumination point. The CIE-1931 RGB colour coordinates (0.67, 0.33) of **CDI 2** (Fig. 1g) in the powder form and after deposition on the thin film exhibited a 100% colour purity for red emission, and it could be used as a red emitter in organic light emitting diodes (OLEDs). The colour purity of **PDI I** (as control) in the solid state was 84% (Fig. S4†).

The red photoluminescence of **CDI 2** encouraged us to investigate the possibility of their AIE properties. The AIE feature of **CDI 2** was evaluated by measuring its photoluminescence spectra in a binary mixture of DMSO–H_2O with different water fractions (f_w). The emission maxima of **CDI 2** exhibited a red shift from 530 to 640 nm with an increase in f_w, revealing the formation of nanoaggregates. When f_w was increased to 20%, the ratiometric ($I_{640\text{ nm}}/I_{530\text{ nm}}$) photoluminescence intensity of **CDI 2** gradually changed. Afterwards, large ratiometric changes (∼14-fold) were observed for f_w up to 80% (Fig. 1h). Accordingly, we prepared a solution of **CDI 2** in DMSO for comparison. As expected, the photoluminescence and the UV-vis spectra of **CDI 2** recorded in DMSO showed an emission wavelength only at 530 nm and an absorption peak at 474/508 nm (Fig. S5 and S11†). In DMSO, the Franck–Condon progression value $A_{0-0}/A_{0-1} \approx 1.34$ indicated a monomer state of CDIs, whereas a value of A_{0-0}/A_{0-1} of ≤0.7 in a 90% water–DMSO mixture indicated an aggregated state of PDIs (Table S1†).

Complimenting the UV-vis and the fluorescence changes on a supramolecular level, we performed an AFM imaging of thin
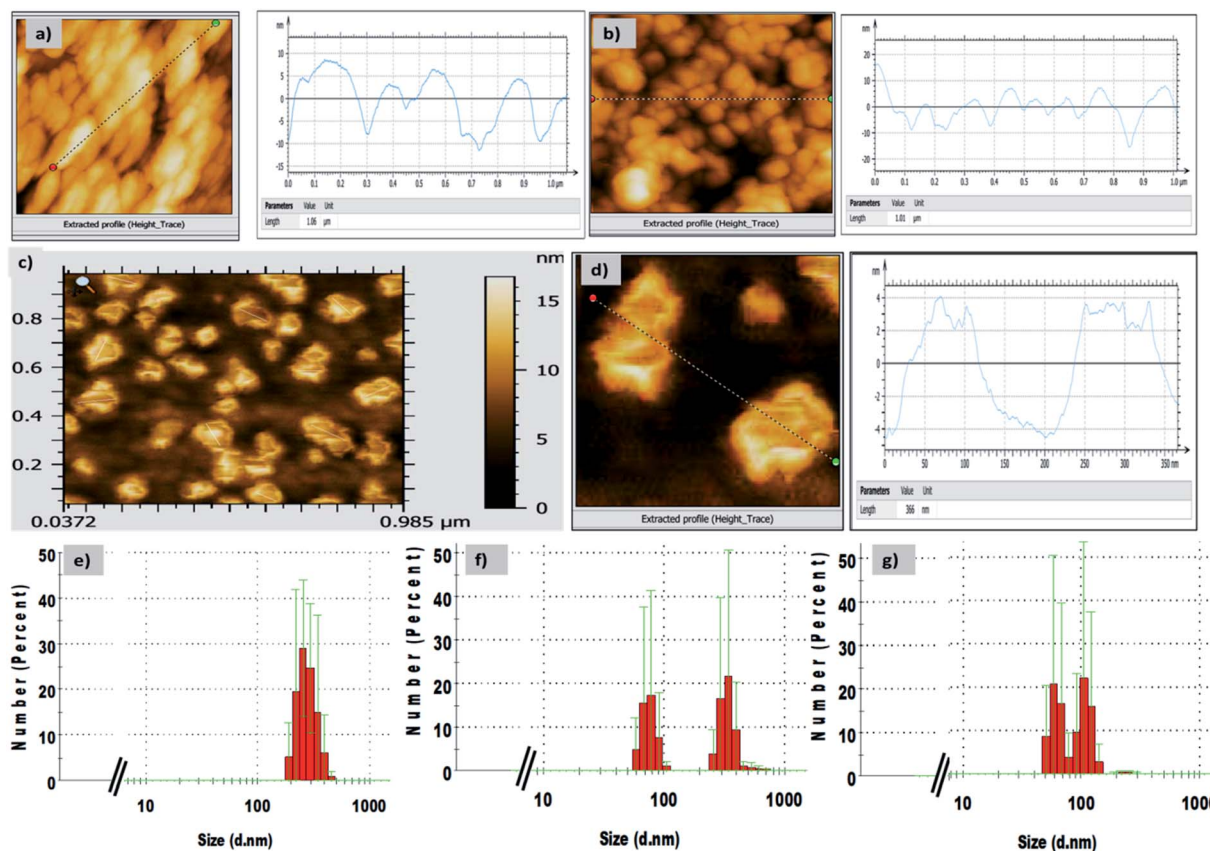
Fig. 2 AFM micrographs of **CDI 2** in (a) DMSO, (b) 50% H_2O/DMSO mixture, (c) 90% H_2O/DMSO mixture and (d) magnified view of (c) showing different morphologies and extracted height profile, size graph of **CDI 2**; DLS bar graph (number percent) of **CDI 2** in (e) DMSO, (f) 50% H_2O/DMSO mixture and (g) 90% H_2O/DMSO mixture.

films prepared on a glass surface using a 10 μM solution of **CDI 2** in DMSO and H_2O–DMSO (f_w = 50% and 90%) (Fig. 2a–d). In DMSO, the formation of oval shape aggregates with a diameter in the range of 240–300 nm over a large surface area was observed (Fig. S6a†). In a 50% H_2O–DMSO binary mixture, the oval aggregates deproliferated into smaller structures and an
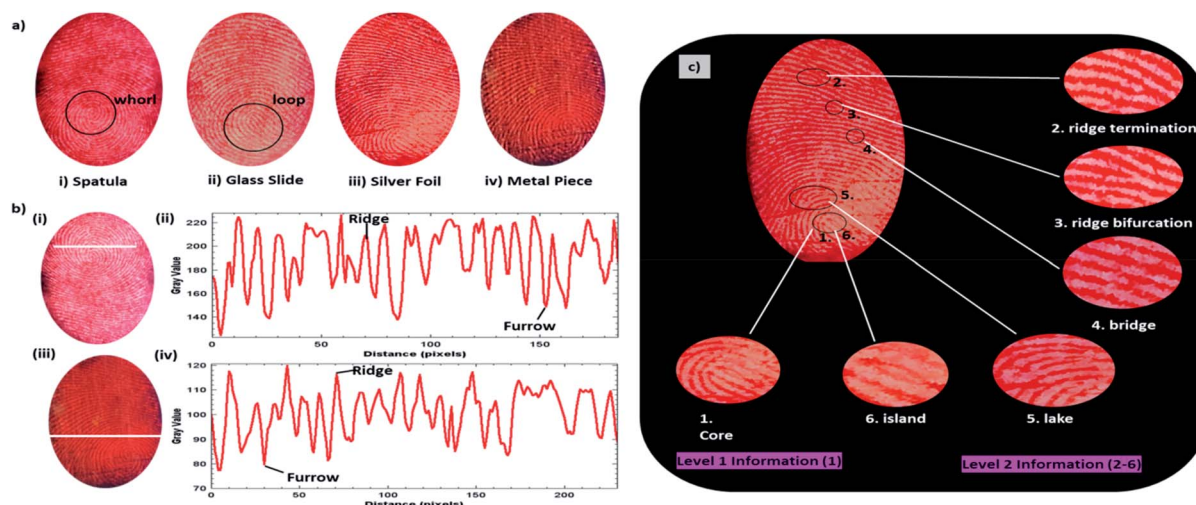

Fig. 3 (a) The fluorescent imaging of LFPs on nonporous surfaces developed with a near-infrared fluorescent compound, namely, **CDI 2** powder. (i) Spatula; (ii) glass slide; (iii) silver foil; and (iv) metal piece under irradiation by 365 nm UV lamp. (b) Photographs of the LFPs developed with the **CDI 2** powder to visualize the latent fingerprints on (i) glass slide and (iii) metal piece; (ii) and (iv) variation in the gray value over the LFP shown by the white line shown in panels (i) and (iii), respectively. (c) Fluorescence image of LFP developed using the **CDI 2** powder-dusting method on the aluminium foil with a 2nd level information providing areas, such as (1) core, (2) ridge termination, (3) ridge bifurcation, (4) bridge, (5) lake and (6) island.

invariant background of oval and sphere aggregates was detected and their diameters slightly decreased to 90–200 nm (Fig. S6b and c†).

Interestingly, in a 90% H_2O–DMSO mixture, the changes in the structures occurred, and we detected a nano-sized inter-linked fibre arranged in such a fashion that it formed a 'bowl' like nano-architecture with a central cavity inside. The invariant clusters of fibres detected on the surface were 70–110 nm in diameter (Fig. 2c and d). The hollow cavity in the centre exhibited a diameter of 138 nm and a depth of ∼2–3 nm (Fig. S6d–f†). We further recorded the dynamic light scattering data for these nanoaggregates in H_2O–DMSO binary mixtures (Fig. 2e–g). In DMSO, **CDI 2** displayed a diameter in the range of 190–530 nm with Z-average and polydispersity index (PDI) values of 353 nm and 0.24, respectively. In the 50% H_2O–DMSO mixture, the size of the aggregates lay in two different sizes, *i.e.* 50–120 nm and 220–531 nm (PDI = 0.29). In the 90% H_2O–DMSO mixture, the size of the nanoaggregates decreased to 80–165 nm, which was in concordance with the AFM data.

The use of near IR-based fluorescent materials in the powder-dusting method for the visualization of LFPs was a simple and non-destructive tool and did not require rigorous post-treatment method (Fig. 3). We applied our **CDI 2** for the development of LFPs on porous and non-porous surfaces, such as ceramic floor tiles, glass, metals, and aluminium foils (Fig. 3a). In all cases, we obtained good quality LFPs to extract information of the ridge pattern (Ist level) and minutae details, such as ridge termination, bifurcation, core, island, lake, and bridge (2nd level) (Fig. 3c). The photoluminescence contrast between the papillary ridges and furrows was analysed by examining the cross-sectional view. The gray value varied significantly over the line/imaginary white line extended on LFPs, thereby clearly showing a discrimination between the ridges and furrows in terms of fluorescence contrast in LFPs (Fig. 3b). The solid-state emission of **CDI 2** was also recorded by directly placing the fingerprint stamped substrate in the spectrofluorometer. The solid-state emission spectrum showed high emission intensity at 660 nm in accordance with the emission maximum of **CDI 2** in solution form. The solid-state emission wavelength of **CDI 2** was further complimented by considering the CIE-1931 RGB colour coordinates. The CIE-1931 RGB colour coordinates (0.67, 0.33) of **CDI 2** on developed LFPs showed 100% colour purity (Fig. 4).
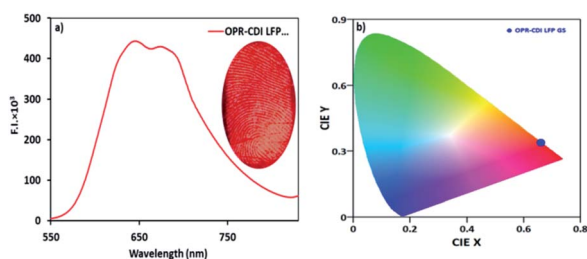
Given that **CDI 2** possessed good emission properties in the solution as well as it contained an oxime group coupled with a propargyl group, **CDI 2** provided heteroatom binding sites, such as O and N. The sensing behaviour of **CDI 2** in the DMSO : HEPES buffer (1 : 9, pH = 7.2) towards numerous metal cations was examined. The fluorescence intensity of **CDI 2** (5 µM) at 640 nm exhibited no detectable changes, whereas the quenching of the fluorescence intensity was observed for Cu^{2+} ions and Pd^0/Pd^{2+} species (Fig. S7†). Later, the detailed response of **CDI 2** towards Cu^{2+} ions and Pd^0/Pd^{2+} species in a 90% aqueous medium was investigated. **CDI 2** (5 µM) exhibited an emission band at 640 nm in the DMSO : HEPES buffer (1 : 9, pH = 7.2, 10^{-2} M) upon excitation at 450 nm. Upon addition of a Pd^0/Pd^{2+} solution (25 µM for Pd^0/50 µM for Pd^{2+}) to **CDI 2** in a 90% buffered medium, the emission intensity at 640 nm was quenched. The Stern–Volmer constant (K_{SV}) values calculated for Pd^0 and Pd^{2+} were 1.74×10^6 M^{-1} and 1.79×10^6 M^{-1}, respectively. The fluorescence response of **CDI 2** towards Pd^{2+}/Pd^0 exhibited a linear relationship (Fig. S8 and S9;† R^2 = 0.98 for Pd^0/Pd^{2+}) between the concentration of Pd^0/Pd^{2+} (0–1 × 10^{-7} M for Pd^0 and 0–1.5 × 10^{-7} M for Pd^{2+}) and the I/I_0 ratio of the fluorescence intensity. The lowest detection limits (LOD) calculated for **CDI 2** towards Pd^0 and Pd^{2+} species were 86.1 nM and 83.9 nM, respectively (Fig. S8 and S9†). Similarly, **CDI 2** (5 µM) could also detect Cu^{2+} ion in the DMSO : HEPES buffer (1 : 9, pH = 7.2, 10^{-2} M) (Fig. S10†). The Cu^{2+} ions tended to bind to the heteroatom binding sites, such as O and N of **CDI 2**. The Stern–Volmer constant (K_{SV}) value for Cu^{2+} was found to be 1.2×10^6 M^{-1}. The quenching of the fluorescence intensity showed a linear correlation of I/I_0 ratio at 640 nm *vs.* Cu^{2+} concentration (0–1 × 10^{-7} M) with a good correlation (R^2 = 0.9912) and a minimal detection limit of 124 nM.

In conclusion, **CDI 2** based 'bowl' nanostructures could be a potential candidate for use as red emitters with a 100% colour purity for OLED applications. **CDI 2** was best for the analysis of latent fingerprints and the detection of important metal ions in a >90% aqueous medium by following the fluorescence approach.

Conflicts of interest

There are no conflicts of interest to declare.

Acknowledgements

Notes and references

1 A. Bécue, *Anal. Methods*, 2016, **8**, 7983–8003.
2 Q. H. Wei, M. Q. Zhang, B. Ogorevc and X. J. Zhang, *Analyst*, 2016, **141**, 6172–6189.

Fig. 4 (a) Emission spectrum of LFP developed with the **CDI 2** powder over a glass slide and (b) CIE-1931 plots corresponding to emission data of (a).

3 P. Rastogi and K. R. Pillai, *J. Indian Acad. Forensic Med.*, 2010, **32**, 11–14.

4 (*a*) J. C. Li, X. J. Zhu, M. Xue, W. Feng, R. L. Ma and F. Y. Li, *Inorg. Chem.*, 2016, **55**, 10278–10283; (*b*) C. L. Chen, Y. Yu, C. G. Li, D. Liu, H. Huang, C. Liang, Y. Lou, Y. Han, Z. Shi and S. H. Feng, *Small*, 2017, **13**, 1702305.

5 (*a*) H. Singh, R. Sharma, G. Bhargava, S. Kumar and P. Singh, *New J. Chem.*, 2018, **42**, 12900–12907; (*b*) P. Singh, H. Singh, R. Sharma, G. Bhargava and S. Kumar, *J. Mater. Chem. C*, 2016, **4**, 11180–11189.

6 M. Srinivasa, G. R. Vijayakumar, K. M. Mahadevan, H. Nagabhushana and H. S. Bhojya Naik, *J. Sci.*, 2017, **2**, 156–164.

7 G. S. Sodhi and J. Kaur, *Forensic Sci. Int.*, 2001, **120**, 172–176.

8 A. Baride, G. Sigdel, W. M. Cross, J. J. Kellar and P. S. May, *ACS Appl. Nano Mater.*, 2019, **7**, 4518–4527.

9 N. Thejokalyani and S. J. Dhoble, *Renew. Sust. Energ. Rev.*, 2014, **32**, 448–467.

10 (*a*) H. Xiang, J. Cheng, X. Ma, X. Zhou and J. J. Chruma, *Chem. Soc. Rev.*, 2013, **42**, 6128–6185; (*b*) K. H. Lee, M. H. Park, B. M. Seo, J. H. Seo, Y. K. Kim and S. S. Yoon, *Mol. Cryst. Liq. Cryst.*, 2011, **550**, 260–269.

11 (*a*) P. Singh, *J. Photochem. Photobiol., A*, 2020, **403**, 112824; (*b*) P. Sharma, S. Kaur, S. Kaur and P. Singh, *Photochem. Photobiol. Sci.*, 2020, **19**, 504–514.

12 (*a*) Q. Shi, E. S. Andreansky, S. R. Marder and S. B. Blakey, *J. Org. Chem.*, 2017, **82**, 10139–10148; (*b*) M. Yoshida, H. Sakai, K. Ohkubo, S. Fukuzumi and T. Hasobe, *J. Phys. Chem. C*, 2018, **122**, 13333–13346.

13 C. Lutke Eversloh, C. Li and K. Mullen, *Org. Lett.*, 2011, **13**, 4148–4150.

14 U. Rohr, P. Schlichting, A. Böhm, M. Gross, K. Meerholz, C. Bräuchle and K. Müllen, *Angew. Chem., Int. Ed.*, 1998, **37**, 1434–1437.

15 K. Kumar, H. Singh, V. Vanita, R. Singh, K. B. Joshi, G. Bhargava, S. Kumar and P. Singh, *Sens. Actuators, B*, 2019, **283**, 651–658.

16 C. Wyman, P.-P. Sloan and P. Shirley, *Journal of Computer Graphics Techniques*, 2013, **2**, 1–11.

17 Y.-F. Wu, Y.-T. Nien, Y.-J. Wang and I.-G. Chen, *J. Am. Ceram. Soc.*, 2012, **95**, 1360–1366.